ARL-TR-8141 • Sep 2017

US Army Research Laboratory

A Modular Framework for 3-Way Electrochromic Switches

by Jennifer M Elward and B Christopher Rinderspacher

NOTICES

Disclaimers

The findings in this report are not to be construed as an official Department of the Army position unless so designated by other authorized documents.

Citation of manufacturer's or trade names does not constitute an official endorsement or approval of the use thereof.

Destroy this report when it is no longer needed. Do not return it to the originator.

ARL-TR-8141 ● SEP 2017

US Army Research Laboratory

A Modular Framework for 3-Way Electrochromic Switches

by Jennifer M Elward
GlaxoSmithKline, Collegeville, PA

B Christopher Rinderspacher
Weapons and Materials Research Directorate, ARL

REPORT DOCUMENTATION PAGE

Form Approved
OMB No. 0704-0188

PLEASE DO NOT RETURN YOUR FORM TO THE ABOVE ADDRESS.

1. REPORT DATE *(DD-MM-YYYY)*	2. REPORT TYPE	3. DATES COVERED (From - To)
September 2017	Technical Report	October 2016–March 2017

4. TITLE AND SUBTITLE
A Modular Framework for 3-Way Electrochromic Switches

5a. CONTRACT NUMBER

5b. GRANT NUMBER

5c. PROGRAM ELEMENT NUMBER

6. AUTHOR(S)
Jennifer M Elward and B Christopher Rinderspacher

5d. PROJECT NUMBER

5e. TASK NUMBER

5f. WORK UNIT NUMBER

7. PERFORMING ORGANIZATION NAME(S) AND ADDRESS(ES)
US Army Research Laboratory
ATTN: RDRL-WMM-G
Aberdeen Proving Ground, MD 21005-5066

8. PERFORMING ORGANIZATION REPORT NUMBER
ARL-TR-8141

9. SPONSORING/MONITORING AGENCY NAME(S) AND ADDRESS(ES)

10. SPONSOR/MONITOR'S ACRONYM(S)

11. SPONSOR/MONITOR'S REPORT NUMBER(S)

12. DISTRIBUTION/AVAILABILITY STATEMENT
Approved for public release; distribution is unlimited.

13. SUPPLEMENTARY NOTES
primary author's email: <berend.c.rinderspacher.civ@mail.mil>

14. ABSTRACT
We present a computational study of a novel molecular framework using an allylic bridge for electrochromic applications. The molecules were studied using density functional theory (DFT) at the CAM-B3LYP/6-31+G(d) level. We report spectra, (hyper)polarizabilities, and deprotonation energies. Large spectral shifts are predicted spanning the visible spectral window. Both transparent–to–colored and colored–to–colored transitions are predicted to be feasible. High polarizabilities indicate further tunability through environmental factors.

15. SUBJECT TERMS
optically adaptable materials, density functional theory, spectroscopy, molecular design

16. SECURITY CLASSIFICATION OF:			17. LIMITATION OF ABSTRACT	18. NUMBER OF PAGES	19a. NAME OF RESPONSIBLE PERSON
a. REPORT	b. ABSTRACT	c. THIS PAGE			B Christopher Rinderspacher
Unclassified	Unclassified	Unclassified	UU	44	19b. TELEPHONE NUMBER (Include area code) 410-306-2811

Contents

List of Figures

List of Tables

INTENTIONALLY LEFT BLANK.

1. Introduction

Many applications in multifunctional materials require a stimulus-controlled reversible change within a material. Examples include photovoltaics,[1] shape memory polymers,[2] self-healing materials,[3] and force responsive luminescent materials.[4] Optically adaptive materials (OAMs), which display an optical signature upon structural change, possess this capability.[5–10] Mechanisms available to control OAM behavior include thermo-, chemo-, photo-, mechano-, and electrochromism.[11–16] Optical response can thus be modulated as a function of changing environmental factors like change in pH[17] or application of low voltage bias.[18] Generally, for this class of materials, environmental changes result in a chemical rearrangement, which can include isomerization, intramolecular hydrogen or group transfers, electrocyclic reactions, and ring opening processes.[19–21] As a result of this environmentally induced structural modification, a significant shift in the absorbance of the material from its original state can take place.

OAMs find application in a variety of fields. Optical switches,[22] frequency filters,[23] variable attenuators,[24] sensors[25–27] and optical displays[28] are all examples of OAM applications. More recently, smart window technology,[29] anti-glare coating for automotive mirrors,[30] and protective eyewear[31] have also put OAMs in the spotlight.

Of particular interest is switching between stable states, such as for smart windows, which adjust their opacity and color under an applied voltage but remain in the switched state even when the field is discontinued. In recent work by Moser et al., single-walled carbon nanotubes have been used as an OAM with applications in smart window technology.[32] Another avenue using pthalocyanine-based polymers was developed by Solis and coworkers. This material has the capability to switch from a green to gray color in its reduced versus oxidized states. The technology has been successfully implemented in a prototype electrochromic window device.[33]

Electrochromic polymer ink is another application relying on switched stable states. Österholm et al.[34] printed e-ink material which switches from a colored to a clear state via ink jet technology, whereas Chen et al. have printed flexible films with electrochromic ink in multiple color switching patterns.[35]

To exploit the full potential of electrochromic applications, a database of electrochromophores with a wide variety of electrochromic responses and secondary

properties is essential. Organic electrochromic species are particularly attractive due to their low weight, high contrast, tunable absorption, wide viewing angle, flexible processability, and potential for low power consumption.[14,20,36–41] The combination of these positive characteristics may lead to new electrochromic materials with properties that can be tuned for individual applications.

When considering the capabilities of an electrochromic material, the type of color switching dictates the type of chemical system necessary to perform the task. In general, colored-to-bleached transitions have shown great success as electrochromic materials and examples of this type include tungsten trioxide (WO_3) thin films, viologens, and Prussian blue based materials.[42–45] In addition to colored-to-bleached transitions, colored state-to-colored state transitions are prominent in electrochromics. Often conducting polymers provide a viable framework for hosting this type of change and Lv et al. provide a comprehensive review of polymeric electrochromic materials, which showcases the many colored transitions possible with these materials.[46] The donor-acceptor structure built into the polymeric materials, which is also found in other optical applications such nonlinear optics,[47,48] provides for exceptional color control between the oxidized and reduced states.[49,50] Transparent-to-colored state transitions are less common in electrochromic materials, but as of late have seen some progress.[51]

However, to develop the next generation of electrochromic materials, the chemical switching methodology, which controls many aspects of electrochromic behavior, must be understood and controlled. A technique that has been used to control this mechanism is to introduce a chemical switching group directly into an existing molecular framework. Popular choices for switches include diaryethenes, azobenzenes, and donor-acceptor type frameworks.

Though there are many switching mechanisms, isomerization is a natural mechanism due to the inherent reversibility and responsiveness to stimuli. For example, cis trans isomerization in diarylethenes is well known to be photochromic in nature.[13,19] Keto-enol tautomerization can also be employed as a chemical switching mechanism.[52] The keto-enol tautomerization process is highly responsive to stimuli like changing the pH of the chemical environment as well as exposure to low voltage current. The enol form can be accessed reversibly through deprotonation of the ketone form of the molecule, thereby introducing a double bond and connect-

ing 2 adjoint π-systems. The newly extended π-system is then responsible for the observed optical response.

The approach in this work is based on manipulating the molecular structure of push-pull chromophores. The structure of the chromophore consists of a π-conjugated bridge flanked by an electron-donating group on one end and an electron-accepting group on the other. These compounds tend to be highly colored because of the conjugation between the electron donating and accepting groups on each end of the molecule. A recently reported key insight was the placement of a chemical switch within the conjugated backbone that can turn on/off the conjugation between the electron donating and accepting groups and thus the molecule can go between a colorless and colored state.[20,52] Compared to previous approaches to electrochromic materials such as conjugated polymers or organometallic complexes, these materials offer a better combination of color intensity and control along with fast response times and good stability.

The primary goal of this work is to introduce and understand a highly flexible and modular approach to tuning electrochromic response. The report is organized as follows. In Section 2 the electrochromic chemical framework and computational details are given, Section 3 gives results of the study of the OAM framework and analysis on underlying factors associated with efficiency, and conclusions are given in Section 4.

2. Computational Methods and Frameworks

All geometry optimizations in this work were performed using density functional theory (DFT) with the CAM-B3LYP functional[53] and the 6-31+G(d) basis set[54–56] as implemented in *Gaussian09* rev. C.01[57] using default convergence criteria. The CAM-B3LYP functional was chosen because it is well known to treat computation of spectra of chromophore molecules accurately.[53,58] In addition, it has been shown previously that range corrected functionals[59,60] are ideal for computation of molecular properties. For consistency, structures were also optimized at the PBE0/6-31+G(d) level[61] and were found to be in agreement with those found with CAM-B3LYP. To determine that the structure is at a minimum, frequency analysis was performed. Using the optimized ground state structure, the molecule's polarizability and first hyperpolarizability were computed in the time-dependent DFT framework. In addition, the UV/visible (Vis) spectra of the molecules were computed within the

framework of time-dependent DFT as implemented in *Gaussian09*.[57]

The general chemical framework studied in the present investigation is pictured in Fig. 1. From this framework, 3 sets of molecules were considered. The first 2 sets substituted R_1, R_2, and R_3 with NO_2- or NMe_2-moieties, where $R_1 \neq R_2$. These substitutions were chosen to incorporate both electron-donating and electron-withdrawing groups on the π-system as well as enabling charge-transfer excitations for potential absorption in the visible range. The second set additionally inserted an acetylene bridge at X_2 in Fig. 1. Graphs of the molecules of sets and 1 and 2 can be found in Figs. 2 and 3, respectively.

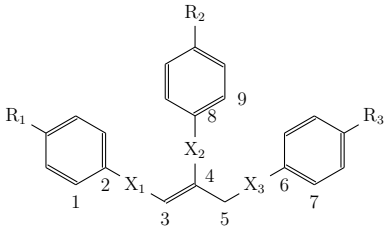

Fig. 1 Electrochromic framework

Because the structure of the electrochromic materials within this study are expected to be highly sensitive to cis-trans-isomerism, both cis and trans structures for each group of substituents have been computed. Structures are labeled in Figs. 2 and 3 as per their conformation and substitution pattern; structures without spacer are given as "X-C" and "X-T", denoting cis and trans, respectively. Structures with spacer are denoted as "X-S-C" and "X-S-T," denoting cis and trans as before and with "S" indicating the acetylene spacer group.

The third set of molecules were selected based on insights from the first 2 sets. These structures are given explicitly in Fig. 4. In structures **5** and **6**, the donor and acceptor moieties were chosen to increase absorption in the 400–700 nm range in the protonated state. Structures **7** and **8** have the same donor-acceptor substitution pattern as structures **5** and **6**; however, acetylene spacer groups have been added at each connecting point. This feature was included to reduce distortion of the π-system due steric hindrance in the vicinity of the allylic bridge as well as extending the π-system for an expected red-shift of the spectra.

Since deprotonation is commonly hypothesized electrochromic mechanism,[20] both

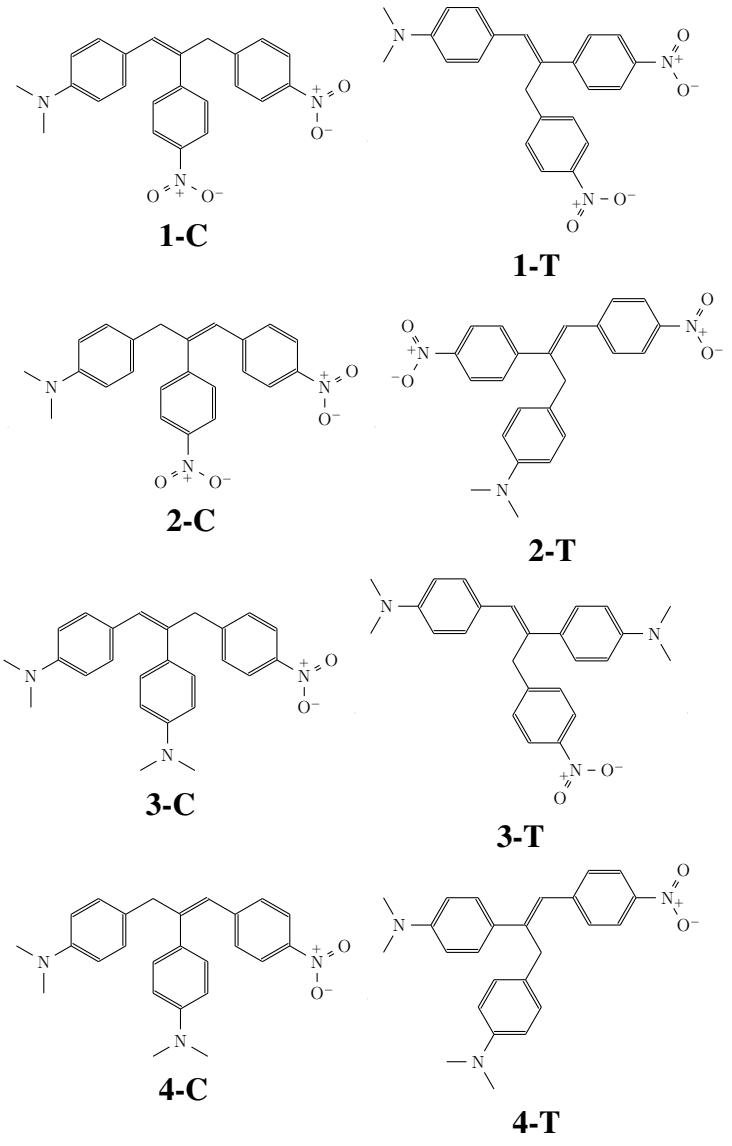

Fig. 2 Molecules in set 1

the protonated and deprotonated states of each molecule were considered. Deprotonation was assumed to occur at the methylene within the allylic bridge. In addition, the effect of reprotonation or a 1-3-hydrogen shift process was assessed for each substitution group combination where these structures are indicated in Figs. 2 and 3.

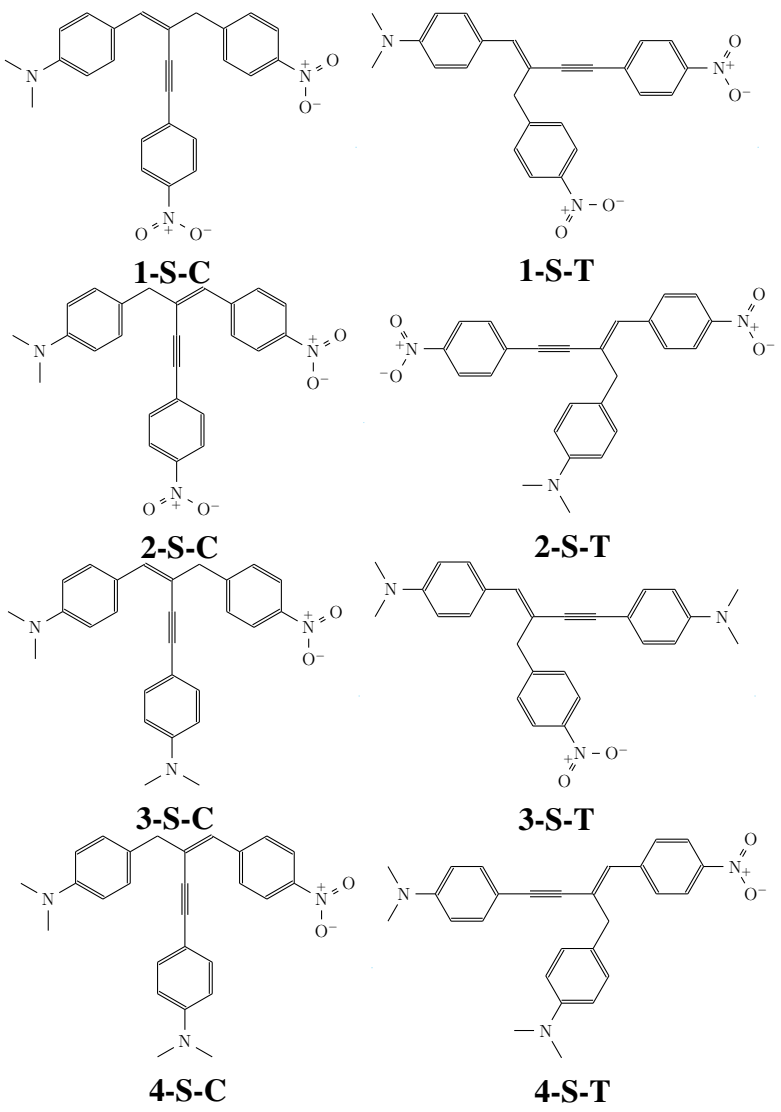

Fig. 3 Molecules in set 2. Same as set 1 except including an acetylene bridge spacer.

3. Results

3.1 Energetics and Structure

The relative ground state energies for the first 2 molecule sets are presented in Table 1. For each set of isomers, the lowest energy is reported as 0.0 eV. The energetic differences are very small, ranging only between 0.0 and 0.16 eV. The cis/trans isomerization energy,

$$E_{C/T} := E_{cis} - E_{trans}, \tag{1}$$

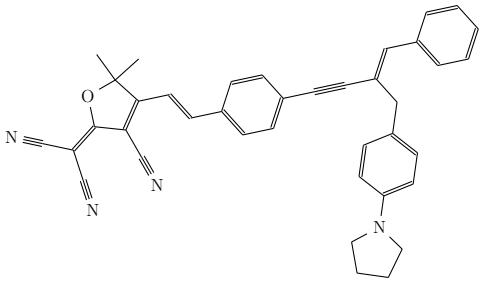

5

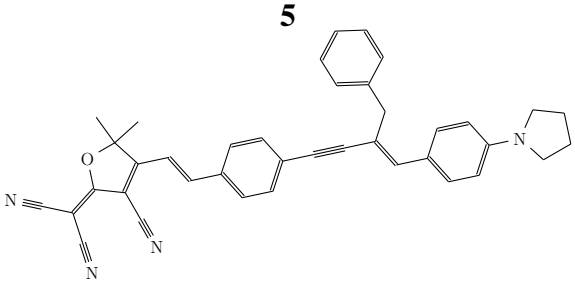

6

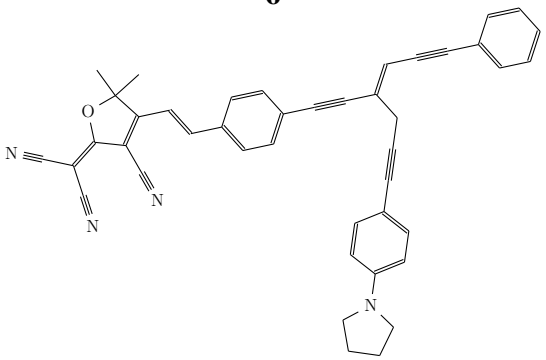

7

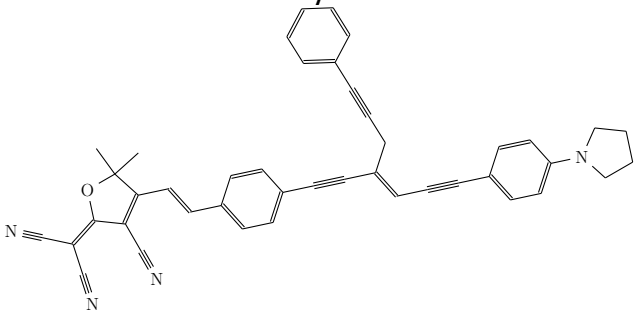

8

Fig. 4 Molecules in set 3

was computed to determine the thermodynamic stabilities. The isomerization energies for each cis/trans pair in molecule sets 1 and 2 are shown in Table 2. In all but 2 groups of isomers, the cis isomer was found to be more stable than the trans isomer. This coincides with the C1-C2-C3-C4 dihedral angle being closer to the fully

planar 180° than the trans isomers are to 0° . In the pairs **1-C/1-T** and **3-C/3-T**, the 2 isomers differ below the chemical accuracy of approximately equal 0.03 eV. In all cases, the isomerization energy is small. The addition of the acetylene spacer group in set 2 causes a greater offset to the cis/trans isomerization energy compared to structures in set 1. Table 3 indicates that the coplanarity of the phenyl-rings with the allylic double bond increases for all compounds in the first 2 sets of molecules. The effect is most dramatic for the dihedral angle between carbons labeled 9, 8, 4, and 3 in Fig. 1. Although the trans isomers in set 2 exhibit more planarity of the π-system, the cis isomer is the more stable isomer. As in set 1, the C1-C2-C3-C4 dihedral angle is closer to planarity; but compared to set 1, the planarity of the C1-C2-C3-C4 dihedral angle increases more for the cis than the trans isomer. A comparison of molecular orbitals (MOs) shows that there is constructive overlap between the acetylene π-MOs perpendicular to the molecular plane and the phenyl π-MOs on R_1.

Table 1 Ground state energies in electronvolts of molecule sets 1 and 2 as well as deprotonation energy ranges in electronvolts

Struc.	E_0/eV	ΔE_{D}/eV
1-C	0.02	14.75 – 14.89
1-T	0.00	14.78 – 14.91
2-C	0.07	14.71 – 14.85
2-T	0.11	14.66 – 14.80
3-C	0.00	15.10 – 15.20
3-T	0.02	15.09 – 15.18
4-C	0.01	15.09 – 15.19
4-T	0.07	15.04 – 15.13
1-S-C	0.00	14.90 – 14.96
1-S-T	0.08	14.82 – 14.88
2-S-C	0.08	14.82 – 14.88
2-S-T	0.16	14.74 – 14.80
3-S-C	0.00	15.22 – 15.28
3-S-T	0.09	15.13 – 15.19
4-S-C	0.04	15.18 – 15.24
4-S-T	0.13	15.09 – 15.15

The primary mechanism for color change in these molecules is assumed to be a deprotonation of the allyl bridge. For the deprotonated states, 4 conformers with R_1 and R_3 being either cis or trans on the allylic bridge with respect to R_2 were optimized. In general, the lowest energy structure was found to be that which had

Table 2 Cis/trans isomerization energies for each cis/trans structural pair in the neutral state of molecule sets 1 and 2

Structure Pair Number	$E_{C/T}$/meV
1	23.604
2	-47.126
3	-18.835
4	-56.404
1-S	-75.539
2-S	-80.180
3-S	-90.175
4-S	-90.677

Table 3 Selected dihedral angles for neutral structures 1 to 4. Labels correspond to the labeling in Fig. 1.

Struc.	1-2-3-4	9-8-4-3	2-3-4-5	2-3-4-8	7-6-5-4	6-5-4-3
1-C	−152.82	−122.90	−176.68	5.22	60.23	−115.97
1-T	37.31	−142.04	5.50	−177.12	25.86	−111.34
2-C	−149.93	−115.29	−179.34	4.79	−63.12	113.79
2-T	−54.41	141.49	−4.17	177.05	45.13	−99.85
3-C	−159.39	−118.83	−177.13	4.97	68.61	−115.26
3-T	47.78	141.19	1.61	−179.80	132.35	124.36
4-C	152.55	123.87	177.02	−5.66	−72.28	113.99
4-T	−47.55	−141.42	−1.73	−179.79	55.18	−123.00
1-S-C	−166.31	−153.48	−179.41	3.13	−53.87	118.06
1-S-T	35.58	−170.15	3.69	−176.72	118.07	135.21
2-S-C	156.60	153.18	179.82	−2.02	64.78	−120.91
2-S-T	−39.45	160.62	−2.97	179.04	68.93	−136.67
3-S-C	−171.31	−155.90	−179.82	1.95	−48.90	118.37
3-S-T	39.41	−163.69	3.87	−176.88	117.34	132.41
4-S-C	162.80	160.89	179.61	−2.84	63.06	−118.63
4-S-T	34.12	179.28	3.20	−179.38	17.72	−103.43

the donor/acceptor pair in trans orientation and the opposing group in the cis orientation. This configuration minimizes steric hindrance around the allyl moiety while allowing full conjugation of the π-system to R_2. The neutral trend of enhanced coplanarity upon insertion of the acetylene spacer group does not apply as reliably in the deprotonated states (Table 4), in part due to generally greater coplanarity in the deprotonated species of compounds **1-C** through **4-T**. But as before the impact of the spacer is greatest on the dihedral angle between carbons labeled 9, 8, 4, and 3 in Fig. 1.

Table 4 Selected dihedral angles for the most stable deprotonated conformer/isomer

Struc.	1-2-3-4	9-8-4-3	2-3-4-5	2-3-4-8	7-6-5-4	6-5-4-3
1/2-X	-153.94	-132.23	-173.33	14.12	9.08	20.59
3/4-X	-23.11	130.57	-11.46	175.07	173.56	156.56
1/2-S-X	170.023	-179.08	164.44	-23.64	-19.55	-9.94
3/4-S-X	-170.94	-177.83	-165.46	21.81	21.25	9.89

The deprotonation energy,

$$\Delta E_{\mathrm{D}} := E_{\text{deprot}} - -E_{\text{neutral}}, \tag{2}$$

is used here as a proxy for estimating the relative ease and speed with which the deprotonation will occur. The deprotonation energy in electronvolts is given as a range for each cis/trans pair as shown in Table 1. Among each set of isomers, the deprotonation energies were similar in their magnitude and, in the absence of a biasing deprotonation mechanism, it is not possible to predict whether there will be a main contributor to the final deprotonated state.

Molecules **1-C** through **2-T** and **1-S-C** through **2-S-T** have similar ΔE_{D} between 14.66-14.96 eV. But, ΔE_{D} for molecules **3-C** through **4-C** and **3-S-C** through **4-S-C** was found to lie between 15.04 and 15.28 eV. This result is consistent with the expectation that a larger number of electron donors in compounds **3** and **4** destabilizes the anion leading to a higher deprotonation energy. Within the context of the electrochromic molecules investigated experimentally in Zhang et al.[52] and assuming that the mechanism of deprotonation is similar, the deprotonation energies for the present compounds are very similar to the reference molecule's deprotonation energy of 14.51 eV.

Adding the acetylene spacer between the allyl bridge and R_2 shifts the deprotonation energy range toward higher values, which is consistent with the expectation that steric crowding around the allylic bridge decreases with the spacer. The steric crowding indeed is found to decrease with the spacer as evidenced by the dihedral angles in Table 4 associated with the coplanarity of the π-system.

3.2 Spectral Properties

To determine the color-change efficiency of the candidate chromophore molecules, the UV/Vis spectra were computed for all species. The excitation wavelengths λ_{max} associated with the respective maximal oscillator strength for both neutral and deprotonated molecules are given in Table 5. The difference between λ_{max} of corresponding states was also evaluated to determine spectral shift and is given in Table 5. λ_{max} is defined as the peak that has the largest oscillator strength and thus the largest intensity. The first excitation wavelength λ_0 does not always coincide with λ_{max}. Table 6 explicitly lists oscillator strengths even when these are below 0.1; but for purposes of comparing λ_0 and λ_{max}, such excitations are not considered significant in the following. Furthermore, isomers deprotonate to the same species. For example, molecules **1-C** and **1-T** (R_1 = $\mathrm{N(CH_3)_2}$, R_3 = $\mathrm{NO_2}$, R_4 = $\mathrm{NO_2}$) deprotonate to the same set of isomers as **2-C** and **2-T** (R_1 = $\mathrm{NO_2}$, R_3 = $\mathrm{NO_2}$, R_4 = $\mathrm{N(CH_3)_2}$). For molecules in sets 1 and 2, they were found to undergo a transparent (or colorless) to colored transition upon deprotonation. Spectral data of the deprotonated species are only provided here for the lowest energy isomer, as the spectra do not vary much.

Table 5 Excitation wavelength, λ_{max}, and maximum oscillator strengths, f, for neutral and deprotonated compounds 1-C – 4-S-C, as well as the induced shift upon deprotonation. Superscripts N and D denote the neutral and deprotonated values, respectively.

Struc.	$\lambda^{\text{N}}_{\text{max}}$	f^{N}	$\lambda^{\text{D}}_{\text{max}}$	f^{D}	$\Delta\lambda_{\text{max}}$
1-C	269	0.52	481	1.02	211
1-T	341	0.80	"	"	139
2-C	295	0.28	"	"	182
2-T	293	0.73	"	"	184
3-C	255	0.43	502	1.04	246
3-T	285	1.02	"	"	216
4-C	341	0.32	"	"	162
4-T	333	0.60	"	"	169
1-S-C	378	0.61	509	0.93	130
1-S-T	358	1.32	"	"	151
2-S-C	336	0.77	"	"	173
2-S-T	333	1.38	"	"	176
3-S-C	331	0.55	528	0.97	197
3-S-T	321	1.51	"	"	207
4-S-C	370	0.64	"	"	158
4-S-T	362	1.25	"	"	166

Table 6 Leading excitation wavelength λ_0 and oscillator strengths f for neutral and deprotonated compounds 1-C – 4-S-C. Superscripts N and D denote the neutral and deprotonated values, respectively.

Struc.	λ_0^{N}	f^{N}	λ_0^{D}	f^{D}
1-C	351	0.20	819	0.06
1-T	341	0.80	"	"
2-C	318	0.12	"	"
2-T	295	0.21	"	"
3-C	286	0.30	502	1.04
3-T	333	0.03[a]	"	"
4-C	341	0.32	"	"
4-T	333	0.60	"	"
1-S-C	378	0.61	927	0.07
1-S-T	358	1.32	"	"
2-S-C	355	0.07[a]	"	"
2-S-T	357	0.03[a]	"	"
3-S-C	350	0.39	528	0.97
3-S-T	352	0.18	"	"
4-S-C	370	0.64	"	"
4-S-T	362	1.25	"	"

[a] not considered significant for purposes of determining λ_0

In the first set of molecules, the maximum oscillator strengths are always greater for the neutral trans configurations with respect to their cis counterparts and $\lambda_{\mathrm{max}} = \lambda_0$ for all neutral compounds in the trans configuration except **3-T**, but λ_0 for the cis configurations is always greater, albeit not always by much (Table 7). The push-pull compounds **1** and **4** exhibit markedly higher λ_0 ranging between 333 and 351 nm than **2** and **3** (285–318 nm), as might be expected despite the poor coplanarity of the bridging π-system. Yet, all spectra remain well outside of the visible range. Simulated spectra of neutral structures **3-C** and **3-T** are shown in Fig. 5. Notably, spectra of the neutral states for both cis and trans geometries are very similar.

Upon deprotonation, λ_{max} increases by 139 to 246 nm into the visible regime, ranging between 481 and 502 nm. For compounds **1** and **2** with an electron acceptor at R_2, λ_0 increases even more considerably into the IR spectrum, but the associated oscillator strengths are very low. Figure 5 includes a simulated spectrum of deprotonated structure **3**. Compared to the neutral structures, there is a significant red-shift of the entire spectrum.

Table 7 Effect of cis/trans isomerism on λ_{max} and λ_0 for neutral structures. Spectral shift is given in nanometers. Equals sign (=) indicates that λ_{max} is equivalent to λ_0.

Struc.	$\Delta\lambda_{max}$	$\Delta\lambda_0$
1	-71	10.18
2	2	23.2
3[a]	< 1	< 1
4	8	=
1-S	20	=
2-S[a]	3	=
3-S	10	2
4-S	8	=

[a]oscillator strength of λ_0 deemed insignificant.

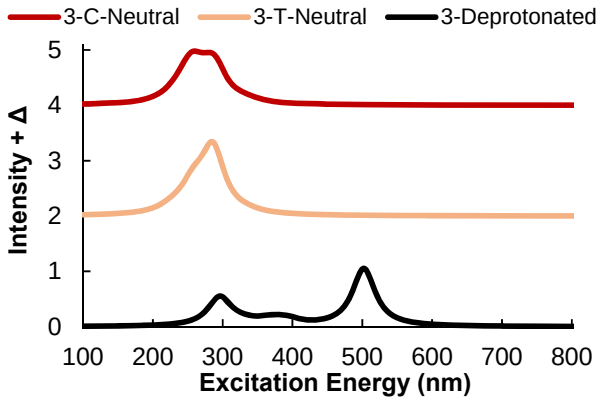

Fig. 5 Spectra for structure 3, both neutral and deprotonated. Structure intensity has been shifted by a chosen Δ for clarity. For the deprotonated spectra (black) Δ = 0, for the neutral trans spectra Δ = 2, and for the neutral cis structure Δ = 4.

Set 2 follows the same trends as set 1 except that $\lambda_0 = \lambda_{\text{max}}$ in all neutral cases but **3-S**. Since λ_0 of all neutral species in set 2 are shifted to the red by 17–64 nm, λ_{max} of the neutral cis species is significantly red-shifted (Table 8). As an example, spectra for structures **1-C** and **1-S-C** are overlaid in Fig. 6. Despite the red-shifts introduced by the acetylene spacer, none of these compounds is predicted to absorb in the visible range, although **1-S-C** with 378 nm comes close. In all cases, the oscillator strengths increased for λ_{max}. λ_{max} of the deprotonated compounds also exhibited a red-shift compared to set 1 by 20–28 nm without leaving the visible

Table 8 Change in λ_0 and λ_{max} as a function of acetylene spacer connecting R_2 to the allyl bridge. (C) denotes cis conformation and (T) denotes trans conformation. $\Delta\lambda = \lambda^{spacer} - -\lambda^{non-spacer}$. Equals sign (=) indicates that $\Delta\lambda_{max}$ and $\Delta\lambda_0$ are equivalent. Deprotonated spectral data compared for lowest energy conformer. Superscripts N and D denote the neutral and deprotonated values, respectively.

Struc.	$\Delta\lambda^N_{max}$	$\Delta\lambda^N_0$	$\Delta\lambda^D_{max}$	$\Delta\lambda^D_0$
1 (C)	109	27	27	107
1 (T)	17	=	()	()
2 (C)	40	18[a]	()	()
2 (T)	40	38[a]	30	98
3 (C)	76	64	27	=
3 (T)	35	67[a]	()	()
4 (C)	30	=	()	()
4 (T)	29	=	28	=

[a]oscillator strength of λ_0 deemed insignificant.

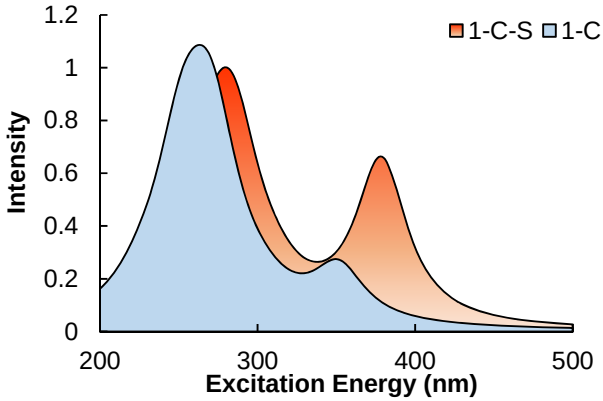

Fig. 6 Spectral overlay of structure 1-C and 1-S-C showcasing the effect of the spacer group

range. Figure 7 shows a comparison of representative spectra of sets 1 and 2.

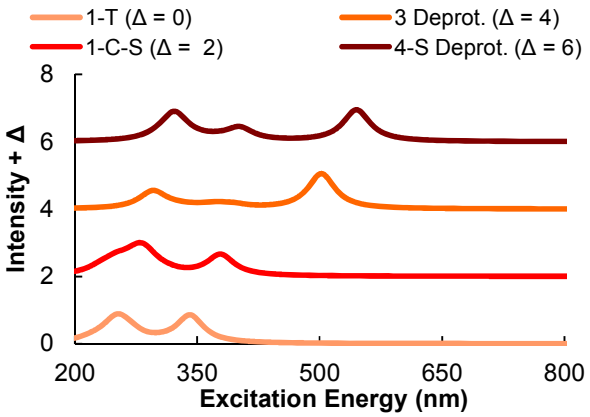

Fig. 7 Spectra for the top 4 performing candidate structures in both non-spacer and spacer groups. Neutral and deprotonated states are given. Spectra are shifted for ease of viewing. The top performing neutral structures are structure 1-T ($\Delta = 0$,λ_{max} = 341 nm, f^N = 0.8) and 1-S-C ($\Delta = 2$, λ_{max} = 378 nm, f^N = 0.6113). The top performing deprotonated structures are structure 3 ($\Delta = 4$, λ_{max} = 502 nm, f^D = 1.04) and structure 4-S ($\Delta = 6$, λ_{max} = 529 nm, f^D = 0.98).

3.3 Molecular Orbital Analysis

The highest occupied molecular orbital (HOMO)→lowest unoccupied molecular orbital (LUMO) transition is the predominant contribution to λ_0 for all structures in sets 1 and 2 with the exception of compound **4-C**. For neutral compounds, the HOMOs concentrate on the donor moieties, while the LUMOs are concentrated around the acceptor moieties, so that this HOMO→LUMO transition indicates a charge transfer process across the donor/acceptor system.

The lack of coplanarity in the extended π-system between R_1 and R_2 for molecules of set 1 manifests itself clearly in the orientations of the phenyl rings adjacent to R_1 and R_2, which are close to perpendicular and whose associated π-MOs are contorted. Figs. 8 and 9 show the typical quality of such HOMOs and LUMOs. Since λ_{max} differs from λ_0 for neutral **3-T** and the neutral cis isomers of set 1 except for **4-C**, but is the same for the other structures, no uniform trend was discovered for λ_{max}. Compounds **1-C** and **2-C** possess 2 possibilities for a donor-to-acceptor charge transfer excitation. One of these transitions corresponds to the HOMO→LUMO transition, whereas λ_{max} corresponds to another. Structure **3-C** has only one acceptor, which is separated from the larger π-system by the methylene moiety. Instead of a charge-transfer excitation, λ_{max} is dominated by a $\pi \rightarrow \pi^*$ transition (HOMO-

5→LUMO) internal to the phenyl moiety attached to R_3. In contrast, the HOMO is a π-orbital spanning R_1, the allyl bridge, and R_2. MOs for **3-C** are given in Fig. 9. Although the HOMO→LUMO transition does not dominate $\lambda_0 = \lambda_{\text{max}}$ for compound **4-C**, the dominating HOMO-1→LUMO transition of λ_0 indicates a strong charge-transfer excitation with considerable contribution from the donor at R_2 (as shown in Fig. 10).

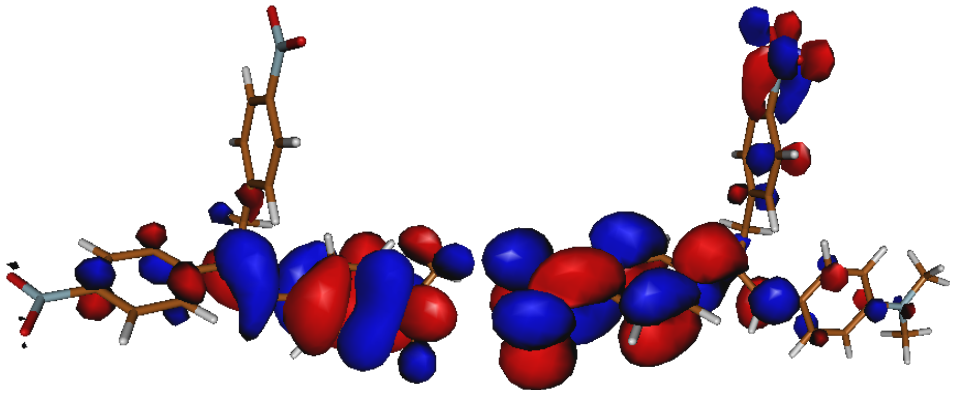

(a) (b)

Fig. 8 HOMO (a) and LUMO (b) for 4-T molecule. In this case $\lambda_{max} = \lambda_0$.

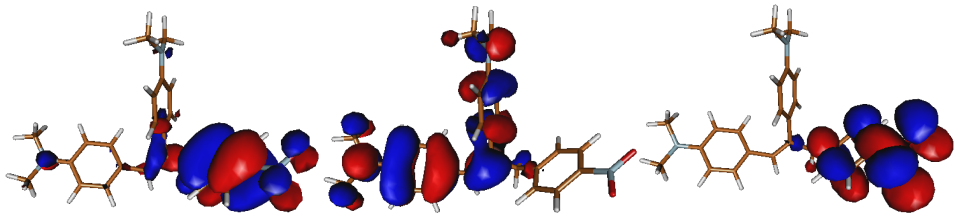

(a) (b) (c)

Fig. 9 HOMO-5 (a), HOMO (b), and LUMO (c) for 3-C molecule. λ_{max} is dominated by a HOMO-5→LUMO transition, whereas λ_0 is dominated by HOMO→LUMO.

In deprotonated structures with the acceptor group in site R_2 (compounds **1** and **2**), there are 2 distinct MO transitions that contribute predominantly to λ_{max} and λ_0. The λ_0 peak is dominated by the HOMO→LUMO transition. The HOMO in these cases has significant allyl anion character, while the LUMO does not, which leads to a charge transfer excitation along the π-system from donor and allyl bridge to the

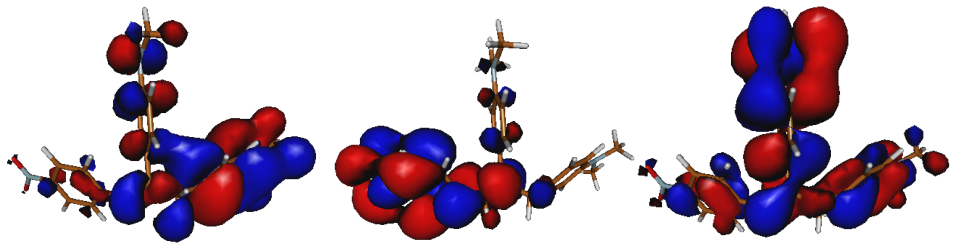

(a) (b) (c)

Fig. 10 Molecular orbitals for molecule 4-C, neutral. HOMO is given in (a), LUMO in (b), and HOMO-1 in (c).

acceptor at R_2. The λ_{max} peak is dominated by the HOMO→LUMO+1 transition, which does not include significant contributions from the donor at R_2. Contrary to the HOMO→LUMO transition, the HOMO→LUMO+1 indicates that λ_{max} is a result of a $\pi \rightarrow \pi^*$ excitation internal to the allyl bridge. Visualization of the MOs are given in Figs. 11 and 12.

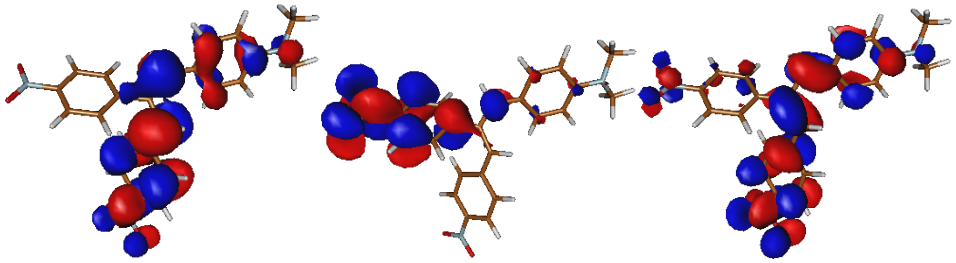

(a) (b) (c)

Fig. 11 HOMO (a), LUMO (b), and LUMO+1 (c) MO diagrams for the lowest energy isomer of deprotonated structures 1 and 2. A HOMO→LUMO transition dominates λ_0 and λ_{max} has the strongest contribution from a HOMO→LUMO+1 transition.

In contrast, compounds **3** and **4** feature a donor group at R_2 instead of an acceptor. Here, too, $\lambda_{\text{max}} = \lambda_0$ is predominantly a HOMO→LUMO transition, but the character is comparable to the HOMO→LUMO+1 λ_{max} transition seen in **1** and **2**.

The main difference between molecules in set 1 and their counterparts in set 2 can be found in the increased coplanarity of π-system adjoining R_1 and R_2. This is particularly reflected in the push-pull systems **1-S** and **4-S**. Their HOMOs show increased contributions from R_2 and diminished contributions from R_3. The LUMOs

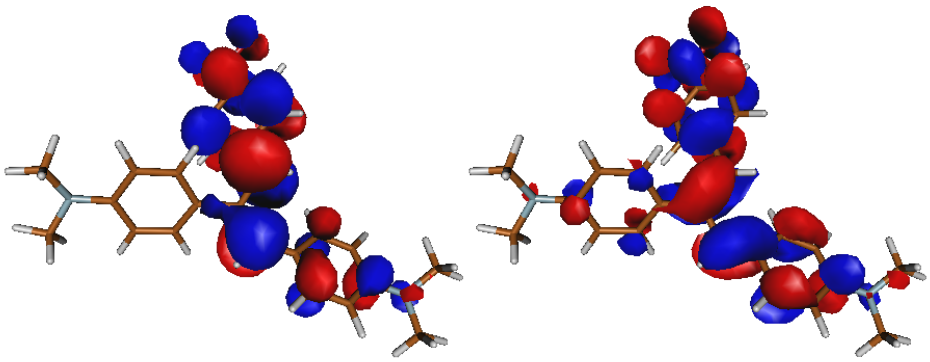

(a) (b)

Fig. 12 HOMO (a) and LUMO (b) MO diagrams for lowest-energy structure of deprotonated 3 and 4. $\lambda_{max} = \lambda_0$ is dominated by a HOMO→LUMO transition.

of **1-S** also show diminished contributions of the second electron-withdrawing nitro-group at R_3. Molecules **4-S** lack a secondary electron-acceptor and don't show any significant qualitative difference in their LUMOs compared to their counterparts in set 1. Molecules **2-S** and **3-S** only show increased planarity of their HOMOs and LUMOs, but no qualitative difference of contributions from the various components.

3.4 Dipole Moments and Polarizabilities

The polarizability plays both a role in transparency as well as any propensity for solvatochromic shifts.[20] Furthermore, the extent of dipole moments dictates the orientability of the electrochromophore in a medium. Table 9 shows the polarizability (α) and dipole moment ($\|\mu\|$) of sets 1 and 2 at the optimized geometries, including both neutral and deprotonated molecular forms. The table also includes hyperpolarizabilities in the dipole direction (β_μ) for the neutral states. Compounds **1** and **4** are an inversion of each other with respect to the donor/acceptor patterns, as are **2** and **3**. In general, the dipole moment decreases for each correspondence with the number of electron donors. The opposite is true of the polarizabilities (e.g., **1-T** has a lower polarizability than **4-T**).

Going from cis to trans increases the dipole moment for the push-pull isomers **1** and **4**, while the converse is true of **2** and **3**. The hyperpolarizability follows this same trend. But, the polarizability is always greater for the trans isomer.

Table 9 Polarizability α and dipole moment $\|\mu\|$ for neutral and deprotonated states of compounds 1-C – 4-S-T and 5 – 8, as well as hyperpolarizabilities β_μ in the dipole direction for neutral states. Deprotonated values are given for lowest energy conformer. Superscripts N and D denote neutral and deprotonated compounds, respectively.

Struc.	$\|\mu^{\mathrm{N}}\|$/D	α^{N}/a.u.	$\beta_\mu^{\mathrm{N}}/10^{-30}\mathrm{cm}^5\mathrm{esu}^{-1}$	$\|\mu^{\mathrm{D}}\|$/D	α^{D}/a.u.
1-C	9.59	322.60	5.78	15.70	460.57
1-T	11.16	340.97	13.24	()	()
2-C	9.91	322.01	4.88	()	()
2-T	3.96	326.36	2.48	()	()
3-C	7.66	340.90	4.34	15.22	472.11
3-T	6.24	348.65	2.02	()	()
4-C	8.53	341.97	6.53	()	()
4-T	9.82	349.91	11.32	()	()
1-S-C	10.63	378.76	13.24	15.78	541.29
1-S-T	13.54	395.48	23.64	()	()
2-S-C	8.63	367.93	7.07	()	()
2-S-T	3.29	381.23	2.68	()	()
3-S-C	7.91	397.36	6.30	14.83	533.47
3-S-T	6.29	408.42	1.76	()	()
4-S-C	8.91	397.04	13.21	()	()
4-S-T	10.56	416.86	25.07	()	()
5	12.877	612.800	39.920	1.152	1544.180
6	19.812	665.740	96.286	12.928	1619.990
7	10.404	714.900	45.441	5.913	1388.140
8	19.735	767.790	122.151	12.426	1375.810

The overall largest dipole moment in set 1 was then found for structure **1-T** at 11.16 D, conversely, the smallest dipole moment was 3.96 D for structure **2-T**. The largest and smallest hyperpolarizability were 13.24 and 2.02x$10^{-30}\mathrm{cm}^5\mathrm{esu}^{-1}$ for compounds **1-T** and **4-C**, respectively. In general, hyperpolarizabilities were very small, as might be expected given the non-planarity of the π-system between donors and acceptors.

Introducing the acetylene bridge at R_2 for set 2 leaves the trends found in set 1 intact. The dipole moment increases for all compounds except **2-S**, and only marginally for the **3-S**, which just as **2-S** does not have push-pull character. The polarizabilities increase in all cases by more than 40 a.u. as may be expected considering the increased coplanarity of the π-system. Similarly, the hyperpolarizability also increases for all molecules except **3-S-T**, but the increases are modest.

In the deprotonated states, the dipole moments are considerably increased, as are

the polarizabilities.

3.5 Set 3

Although sets 1 and 2 showed potential for an electrochromic transition from clear to a colored state, the range is limited to small deviations around 500 nm for the deprotonated state. We hypothesized that introducing a stronger electron acceptor would produce a red-shift for both states. Since the isomerization energies for sets 1 and 2 are so low, only the trans isomer was considered. Hence, NO_2 was replaced by the tricyanofurane (TCF) acceptor while one donor was replaced by pyrrolidine and the other by hydrogen, to give molecules **5** and **6** in Fig. 4.

Furthermore, the introduction of the acetylene bridge in set 2 precipitated a significant red-shift in the spectra of both the neutral and deprotonated states. Taking this into account, we hypothesized that adding additional spacer groups to the framework will increase the planarity of the π-system and modify the neutral spectra in a manner that brings the λ_{max} peak beyond 400 nm. This second modification leads to molecules **7** and **8**.

As Table 10 shows, substitution with TCF alone has no significant impact on the coplanarity of the π-system compared to the trans isomers in set 2, as indicated by the high dihedral angle between C1-C2-C3-C4. The added acetylene bridges in **7** and **8** show the expected effect of flattening out the molecule to considerable coplanarity of the π-system. The deprotonated structures of **5** and **6** flatten also, but no further flattening of the π-system between R_1 and R_2 is observed (Table 11).

Table 10 Selected dihedral angles for neutral structures 5 to 8. Labels correspond to the labeling in Fig. 1

Struc.	1-2-3-4	9-8-4-3	2-3-4-5	2-3-4-8	7-6-5-4	6-5-4-3
5	39.08	−160.29	2.92	−179.13	107.62	138.10
6	−33.79	169.91	−3.71	177.32	64.84	−137.90
7	0.93	−167.51	−0.95	178.30	88.76	160.81
8	4.64	177.63	1.42	−179.35	49.00	−118.87

Energetically (Table 12), the increased coplanarity coincides with a considerable stabilization (1.74 eV) of the push-pull molecule **8** over **7**, whereas isomers **5** and **6** follow the trend of sets 1 and 2, where isomers have comparable energies. Con-

Table 11 Selected dihedral angles for the most stable deprotonated conformer/isomer.

Struc.	1-2-3-4	9-8-4-3	2-3-4-5	2-3-4-8	7-6-5-4	6-5-4-3
5	−104.33	−154.70	7.51	−177.23	−168.65	−170.72
6	−14.19	156.29	−8.13	168.39	0.24	−50.16
7	6.39	174.67	15.26	−165.41	5.85	13.50
8	2.90	−179.51	0.34	−179.56	−179.76	179.78

sequently, the deprotonation energies are virtually identical for **5** and **6**. On the other hand, **7** enjoys a much lower deprotonation energy (13.14 eV) than **8** or any other molecules investigated in this work. Despite the stronger electron acceptor, the deprotonation energies for **5** and **6** counterintuitively exceed the deprotonation energies observed in sets 1 and 2.

Table 12 Computed ground state energy for neutral and deprotonated states given in Hartrees. Deprotonation energy is computed following the expression given in Eq. 2 and given in electronvolts.

Struc.	E_{N}/eV	ΔE_{D}/eV
5	0.0	15.48
6	0.5	15.53
7	1.74	13.14
8	0.0	14.88

As Table 13 shows, there is a marked difference between λ_{max} found in sets 1 and 2 and those found in set 3. All molecules in set 3 in the neutral state exhibit λ_{max} between 411-451 nm, with an oscillator strength of 1.8 and greater. Except for **5**, this was also the leading nonnegligible excitation. Both peak location and intensity are significantly increased compared to structures in sets 1 and 2, despite replacing one donor group by hydrogen. Structure **8** has the highest λ_{max} at 451 nm closely followed by **6** (446 nm). Both are conjugated push-pull compounds, which are expected to have high absorption wavelengths and intensities.

In general, the deprotonated absorbance peaks are well separated from the neutral state. Deprotonation was assumed not to change bonding from trans to cis. In each case, a significant red shift was observed from neutral to deprotonated state, reaching a shift of 194 nm at the highest point. The spectra for set 3 can be found in Fig. 13. For each molecule, the overlap between the neutral state absorption spectrum and deprotonated state absorption spectrum is small. The addition of further acety-

Table 13 λ_{max} in nanometers as computed for neutral and deprotonated molecules of set 3, oscillator strengths (f) are given for each state. Deprotonation is assumed not to change bonding from trans to cis. Shift between neutral and deprotonated states is given in nanometers. "=" indicates $\lambda_{\mathbf{max}} = \lambda_0$. Superscript N and D denote neutral and deprotonated species, respectively.

Struc.	$\lambda^{\mathrm{N}}_{\mathrm{max}}$	f^{N}	λ^{N}_{0}	f^{N}	
5	411	1.80	429	0.18	
6	446	2.06	=	=	
7	433	2.10	493	0.00[a]	
8	451	2.46	=	=	
Struc.	$\lambda^{\mathrm{D}}_{\mathrm{max}}$	f^{D}	λ^{D}_{0}	f^{D}	$\Delta\lambda_{\mathrm{max}}$
5	587	0.97	9528	0.02[a]	175
6	586	1.16	8510	0.02[a]	173
7	602	1.10	8424	0.00[a]	194
8	595	1.44	7610	0.01[a]	143

[a]deemed insignificant

lene bridges produces a modest red-shift, but a respectable increase in oscillator strength.

Polarizabilities, hyperpolarizabilities, and dipole moments for set 3 can be found in Table 9. Compared to **1-S-T** and **4-S-T**, dipole moments ($\approx$ 20 D) and polarizabilities (600–800 a.u.) of **6** and **8** are larger by almost a factor of 2. Although polarizabilities for **5** and **7** remain high, their respective dipole moments remain low ($\approx$ 10 D). The dipole moments are insensitive to the acetylene bridges, but the polarizabilities experience another boost of roughly 100 a.u. upon addition of the acetylene bridges. Similar to the linear polarizabilities, the hyperpolarizabilities are higher, especially in the case of structures **6** and **8**.

In the deprotonated states, the polarizabilities are even larger by almost a factor of 2, but dipole moments diminish. The polarizabilities of the deprotonated species also show an inverted sensitivity to addition of the acetylene bridges; **8** and **7** exhibit lower polarizabilities than either **6** and **5**.

As in sets 1 and 2, the MOs and their contributions to λ_{max} were evaluated. As a characteristic example for set 3, MOs for structure **8** are shown in Fig. 14. Only the contribution from the HOMO and HOMO-1 orbitals are pictured as the LUMO for both neutral and deprotonated states are nearly identical in nature.

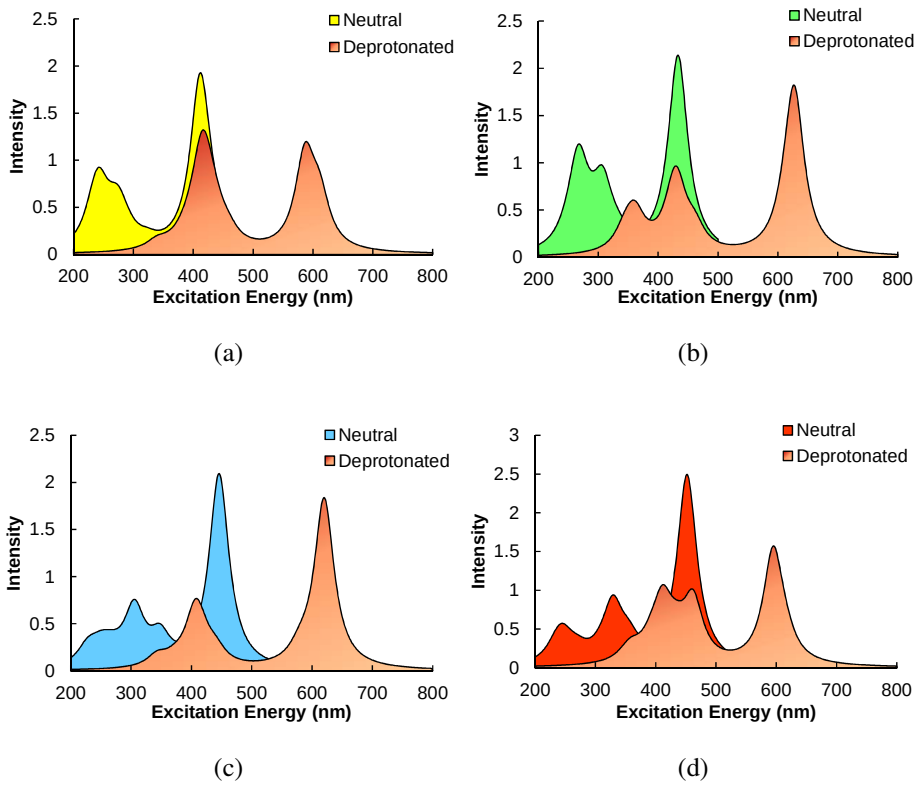

Fig. 13 Computed spectra for chromophores 5 (a), 6 (c), 7 (b), and 8 (d). Both neutral and deprotonated states are shown. Deprotonation is assumed not to change bonding from trans to cis.

The major contribution to the strong λ_{max} transition in **8** is the result of a direct HOMO→LUMO transition. This transition shows charge-transfer character with the HOMO occupying mostly the donor and the LUMO residing predominantly on the acceptor.

Similar to what has been shown in sets 1 and 2, the deprotonated states possess 2 important transitions: HOMO→LUMO and HOMO-1→LUMO. Both HOMO and HOMO-1 are spread out predominantly over the π-system between the R_1 and R_3 sites. While the HOMO-1 is concentrated on the donor, the HOMO is dominated by the allylic bridge. Thus, charge transfer takes place when transitioning to the LUMO in either case. But as Table 13 indicates, the HOMO→LUMO transition shows a negligible oscillator strength, whereas the HOMO-1→LUMO transition leads to the maximal oscillator strength.

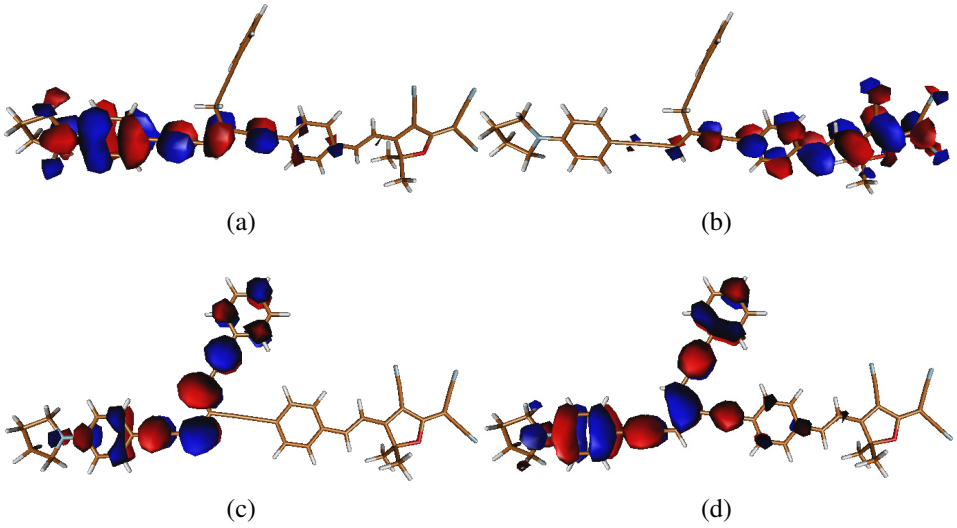

Fig. 14 MOs for structure 8. (a) HOMO-neutral, (b) LUMO-neutral, (c) HOMO deprotonated, and (d) HOMO-1 deprotonated. The LUMO for the deprotonated structure has very similar character in both neutral and deprotonated states.

4. Conclusions

Despite major contortions of the π-system, set 1 remains a viable class for electrochromic interactions showing a transparent-to-colored transition. The contortions may be attributed to the steric interference adjacent to the allyl bridge. This same interference leads to a preference for the cis configurations, which avoids steric clashes between the R_1 and R_3 branches on the allyl bridge. Adding the acetylene bridge to produce set 2 reduces the steric hindrance only between R_1 and R_2, but not between R_1 and R_3, which increases the stability of the cis isomer over the trans isomer even more. Surprisingly, the push-pull isomers in the trans configuration on the allylic double bond are not energetically the most favored. This can be rationalized by reduced steric hindrance in set 1, but for set 2 the observed constructive overlap in MOs between the acetylene π-bonds and the phenyl ring attached to R_3 may contribute as well. Set 3 further supports this explanation as the R_3 branch also shows a preferred proximity to the acetylene bridge attached to R_2. The importance of steric hindrance in sets 1 and 2 is highlighted particularly by **7** and **8**, for which the trans-configured push-pull compound **8** is far more stable than the other isomers.

Relieving the steric hindrance by going to set 2 provides an avenue for positioning

the color of the deprotonated state at the cost of increasing the deprotonation energy, since the acetylene bridge relieves more steric hindrance for the neutral than the deprotonated species. But, the deprotonation energies still remain in the vicinity of deprotonation energies associated with keto-enol species. Going to set 3 lowers the deprotonation energy again for **7** and **8** as well as providing a system for a colored-to-colored transition.

The polarizabilities of all sets were large on the whole and indicate another variable for finetuning the electrochromic response through inclusion in polar media. Although dipoles were considerable, hyperpolarizabilities were relatively small except for **7**. With the right modifications, these may be amplified.

The lack of importance of the donor on the spectrum of the deprotonated species can be explained by the fact that the allyl anion takes on the role of the electron donor as indicated by MOs in the deprotonated states. This implies that the neutral spectrum can be effectively designed by the choice of donor independently because the allyl anion effectively supersedes the donor in the deprotonated state.

In conclusion, we have explored several novel chromophore molecules that show promising characteristics for performance as electrochromic optically adaptable materials. The framework provides many opportunities for further tuning and optimizing[62] of spectra as well as deprotonation energies and even other applications such as nonlinear optics.

5. References

1. Thompson BC, Kim YG, McCarley TD, Reynolds JR. Soluble narrow band gap and blue propylenedioxythiophene-cyanovinylene polymers as multifunctional materials for photovoltaic and electrochromic applications. Journal of the American Chemical Society. 2006;128(39):12714–12725.

2. Behl M, Razzaq MY, Lendlein A. Multifunctional shape-memory polymers. Advanced Materials. 2010;22(31):3388–3410.

3. Shchukin DG, Möhwald H. Self-repairing coatings containing active nanoreservoirs. Small. 2007;3(6):926–943.

4. Teng MJ, Jia XR, Yang S, Chen XF, Wei Y. Reversible tuning luminescent color and emission intensity: a dipeptide-based light-emitting material. Advanced Materials. 2012;24(9):1255–1261.

5. Rosseinsky D, Mortimer R. Electrochromic systems and the prospects for devices. Advanced Materials. 2001;13(11):783+.

6. Argun A, Aubert P, Thompson B, Schwendeman I, Gaupp C, Hwang J, Pinto N, Tanner D, MacDiarmid A, Reynolds J. Multicolored electrochromism polymers: structures and devices. Chem Mater. 2004;16(23):4401–4412.

7. Mortimer R, Dyer A, Reynolds J. Electrochromic organic and polymeric materials for display applications. Displays. 2006;27(1):2–18.

8. Minkin V. Photo-, thermo-, solvato-, and electrochromic spiroheterocyclic compounds. Chem Rev. 2004;104(5):2751–2776.

9. Beaujuge PM, Amb CM, Reynolds JR. Spectral engineering in pi-conjugated polymers with intramolecular donor-acceptor interactions. Acc Chem Res. 2010;43(11):1396–1407.

10. Argun A, Cirpan A, Reynolds J. The first truly all-polymer electrochromic devices. Advanced Materials. 2003;15(16):1338+.

11. Luo X, Li J, Li C, Heng L, Dong YQ, Liu Z, Bo Z, Tang BZ. Reversible switching of the emission of diphenyldibenzofulvenes by thermal and mechanical stimuli. Advanced Materials. 2011;23(29):3261+.

12. Wang M, Koski KJ. Reversible chemochromic MoO_3 nanoribbons through zerovalent metal intercalation. ACS Nano. 2015;9(3):3226–3233.

13. Tian H, Yang S. Recent progresses on diarylethene based photochromic switches. Chemical Society Reviews. 2004;33(2):85–97.

14. Sou K, Chan LY, Lee CLK. Photo-switchable and self-erasable fluorescent nanoprobe. Journal of Photochemistry and Photobiology A: Chemistry. 2017;332:25–31.

15. Chi Z, Zhang X, Xu B, Zhou X, Ma C, Zhang Y, Liu S, Xu J. Recent advances in organic mechanofluorochromic materials. Chem Soc Rev. 2012;41(10):3878–3896.

16. Mortimer RJ. Electrochromic materials. Chem Soc Rev. 1997;26(3):147–156.

17. Xu B, Xu L, Gao G, Yang Y, Guo W, Liu S, Sun Z. Multicolor electrochromic and pH-sensitive nanocomposite thin film based on polyoxometalates and polyviologen. Electrochimica Acta. 2009;54(8):2246–2252.

18. Thompson BC, Schottland P, Zong K, Reynolds JR. In situ colorimetric analysis of electrochromic polymers and devices. Chemistry of Materials. 2000;12(6):1563–1571.

19. Irie M. Diarylethenes for memories and switches. Chemical Reviews. 2000;100(5):1685–1716.

20. Zhang YM, Wang X, Zhang W, Li W, Fang X, Yang B, Li M, Zhang SXA. A single-molecule multicolor electrochromic device generated through medium engineering. Light: Science & Applications. 2015;4(2):e249.

21. Ling Y, Xiang C, Zhou G. Multicolored electrochromism from benzodipyrrolidone-based ambipolar electrochromes at a fixed potential. Journal of Materials Chemistry C. 2017;5(2):290–300.

22. Molten P, Kremers M, Griessen R. Optical switching of y-hydride thin film electrodes a remarkable electrochromic phenomenon. Journal of the Electrochemical Society. 1996;143(10):3348–3353.

23. Baloukas B, Lamarre JM, Martinu L. Electrochromic interference filters fabricated from dense and porous tungsten oxide films. Solar Energy Materials and Solar Cells. 2011;95(3):807–815.

24. Dyer AL, Grenier CR, Reynolds JR. A poly (3, 4-alkylenedioxythiophene) electrochromic variable optical attenuator with near-infrared reflectivity tuned independently of the visible region. Advanced Functional Materials. 2007;17(9):1480–1486.

25. Pellitero MA, Guimerà A, Kitsara M, Villa R, Rubio C, Lakard B, Doche ML, Hihn JY, del Campo FJ. Quantitative self-powered electrochromic biosensors. Chemical Science. 2017.

26. Kim G, Cho S, Chang K, Kim WS, Kang H, Ryu SP, Myoung J, Park J, Park C, Shim W. Spatially pressure-mapped thermochromic interactive sensor. Advanced Materials. 2017.

27. Lee K, Fang YK, Lee WJ, Ho JJ, Chen K, Liao K. Novel electrochromic devices (ECD) of tungsten oxide (WO_3) thin film integrated with amorphous silicon germanium photodetector for hydrogen sensor. Sensors and Actuators B: Chemical. 2000;69(1):96–99.

28. Cho SI, Kwon WJ, Choi SJ, Kim P, Park SA, Kim J, Son SJ, Xiao R, Kim SH, Lee SB. Nanotube-based ultrafast electrochromic display. Advanced Materials. 2005;17(2):171–175.

29. Cai G, Darmawan P, Cheng X, Lee PS. Inkjet printed large area multifunctional smart windows. Advanced Energy Materials. 2017.

30. So S, Fung HWM, Kartub K, Maley AM, Corn RM. Fabrication of pedot nanocone arrays with electrochemically modulated broadband antireflective properties. The Journal of Physical Chemistry Letters. 2017.

31. Österholm AM, Shen DE, Kerszulis JA, Bulloch RH, Kuepfert M, Dyer AL, Reynolds JR. Four shades of brown: tuning of electrochromic polymer blends toward high-contrast eyewear. ACS Applied Materials & Interfaces. 2015;7(3):1413–1421.

32. Moser ML, Li G, Chen M, Bekyarova E, Itkis ME, Haddon RC. Fast electrochromic device based on single-walled carbon nanotube thin films. Nano Lett. 2016;16(9):5386–5393.

33. Solis C, Baigorria E, Milanesio ME, Morales G, Durantini EN, Otero L, Gervaldo M. Electrochemical polymerization of edot modified phthalocyanines and their applications as electrochromic materials with green coloration, and strong absorption in the near-IR. Electrochim Acta. 2016;213:594–605.

34. Österholm AM, Shen DE, Gottfried DS, Reynolds JR. Full color control and high-resolution patterning from inkjet printable cyan/magenta/yellow colored-to-colorless electrochromic polymer inks. Advanced Materials Technologies. 2016.

35. Chen BH, Kao SY, Hu CW, Higuchi M, Ho KC, Liao YC. Printed multicolor high-contrast electrochromic devices. ACS Applied Materials & Interfaces. 2015;7(45):25069–25076.

36. Ko HC, Kang M, Moon B, Lee H. Enhancement of electrochromic contrast of poly (3, 4-ethylenedioxythiophene) by incorporating a pendant viologen. Advanced Materials. 2004;16(19):1712–1716.

37. Sun N, Meng S, Zhou Z, Yao J, Du Y, Wang D, Zhao X, Zhou H, Chen C. High-contrast electrochromic and electrofluorescent dual-switching materials based on 2-diphenylamine-(9, 9-diphenylfluorene)-functionalized semi-aromatic polymers. RSC Advances. 2016;6(70):66288–66296.

38. Tahara H, Baba R, Iwanaga K, Sagara T, Murakami H. Electrochromism of a bipolar reversible redox-active ferrocene-viologen linked ionic liquid. Chem Commun. 2017;53(16):2455–2458.

39. Teran NB, Reynolds JR. Discrete donor-acceptor conjugated systems in neutral and oxidized states: implications toward molecular design for high contrast electrochromics. Chem Mater. 2017.

40. Usha K, Sivakumar R, Sanjeeviraja C, Sathe V, Ganesan V, Wang T. Improved electrochromic performance of a radio frequency magnetron sputtered NiO thin film with high optical switching speed. RSC Advances. 2016;6(83):79668–79680.

41. Xu T, Walter EC, Agrawal A, Bohn C, Velmurugan J, Zhu W, Lezec HJ, Talin AA. High-contrast and fast electrochromic switching enabled by plasmonics. Nature Communications. 2016;7.

42. Mortimer RJ, Reynolds JR. In situ colorimetric and composite coloration efficiency measurements for electrochromic prussian blue. Journal of Materials Chemistry. 2005;15(22):2226–2233.

43. Baeck SH, Choi KS, Jaramillo TF, Stucky GD, McFarland EW. Enhancement of photocatalytic and electrochromic properties of electrochemically fabricated mesoporous WO_3 thin films. Advanced Materials. 2003;15(15):1269–1273.

44. Lin RG, Xu G, Wang MS, Lu G, Li PX, Guo GC. Improved photochromic properties on viologen-based inorganic-organic hybrids by using π-conjugated substituents as electron donors and stabilizers. Inorganic Chemistry. 2013;52(3):1199–1205.

45. Yuksel R, Ataoglu E, Turan J, Alpugan E, Ozdemir Hacioglu S, Toppare L, Cirpan A, Emrah Unalan H, Gunbas G. A new high-performance blue to transmissive electrochromic material and use of silver nanowire network electrodes as substrates. Journal of Polymer Science Part A: Polymer Chemistry. 2017.

46. Lv X, Li W, Ouyang M, Zhang Y, Wright DS, Zhang C. Polymeric electrochromic materials with donor-acceptor structures. Journal of Materials Chemistry C. 2017;5(1):12–28.

47. Rinderspacher BC, Andzelm JW, Rawlett AM, Dougherty JM, Baranoski M, Davis MC. The role of aromatic π-bridges in push-pull-chromophores on the transparency-hyperpolarizability tradeoff. Chem Phys Lett. 2011;507(4–6):221–225.

48. Rinderspacher BC. Electro-optic and spectroscopic properties of push-pull-chromophores with non-aromatic pi-bridges. Chem Phys Lett. 2013;585:21–26.

49. Kerszulis JA, Bulloch RH, Teran NB, Wolfe RM, Reynolds JR. Relax: a sterically relaxed donor-acceptor approach for color tuning in broadly absorbing, high contrast electrochromic polymers. Macromolecules. 2016;49(17):6350–6359.

50. Shao S, Shi J, Murtaza I, Xu P, He Y, Ghosh S, Zhu X, Perepichka IF, Meng H. Exploring the electrochromic properties of poly (thieno [3, 2-b] thiophene) s decorated with electron-deficient side groups. Polymer Chemistry. 2017.

51. Kaabi KA, Wade CR, Dinca M. Transparent-to-dark electrochromic behavior in naphthalene diimide based mesoporous MOF 74 analogs. Chem. 2016;1(2):264–272.

52. Zhang YM, Li M, Li W, Huang Z, Zhu S, Yang B, Wang XC, Zhang SXA. A new class of "electro-acid/base"-induced reversible methyl ketone colour switches. J Mater Chem C. 2013;1:5309–5314.

53. Yanai T, Tew DP, Handy NC. A new hybrid exchange-correlation functional using the coulomb-attenuating method (CAM-B3LYP). Chem Phys Lett. 2004;393(1):51–57.

54. Hehre WJ, Ditchfield R, Pople JA. Self-consistent molecular orbital methods. xii. further extensions of gaussian-type basis sets for use in molecular orbital studies of organic molecules. The Journal of Chemical Physics. 1972;56(5):2257–2261.

55. Hariharan PC, Pople JA. The influence of polarization functions on molecular orbital hydrogenation energies. Theoretical Chemistry Accounts: Theory, Computation, and Modeling (Theoretica Chimica Acta). 1973;28(3):213–222.

56. Clark T, Chandrasekhar J, Spitznagel GW, Schleyer PVR. Efficient diffuse function-augmented basis sets for anion calculations. iii. the 3-21+g basis set for first-row elements, Li–F. Journal of Computational Chemistry. 1983;4(3):294–301.

57. Frisch MJ et al. Gaussian 09 Revision C.01. Wallingford (CT): Gaussian Inc.; 2009.

58. Andzelm J, Rinderspacher BC, Rawlett A, Dougherty J, Baer R, Govind N. Performance of DFT methods in the calculation of optical spectra of TCF-chromophores. J Chem Theory Comput. 2009;5(10):2835–2846.

59. Ruggiero MT, Gooch J, Zubieta J, Korter TM. Evaluation of range-corrected density functionals for the simulation of pyridinium-containing molecular crystals. The Journal of Physical Chemistry A. 2016;120(6):939–947.

60. Quertinmont J, Carletta A, Tumanov NA, Leyssens T, Wouters J, Champagne B. Assessing density functional theory approaches for predicting the structure and relative energy of salicylideneaniline molecular switches in the solid state. The Journal of Physical Chemistry C. 2017.

61. Adamo C, Barone V. Toward reliable density functional methods without adjustable parameters: The PBE0 model. The Journal of Chemical Physics. 1999;110(13):6158–6170.

62. Elward JM, Rinderspacher BC. Smooth heuristic optimization on a complex chemical subspace. Phys Chem Chem Phys. 2015;17:24322–24335.

List of Symbols, Abbreviations, and Acronyms

DFT density functional theory

ECM electrochromic material

HOMO highest occupied molecular orbital

LUMO lowest unoccupied molecular orbital

MO molecular orbital

OAM optically adaptive material

TCF tricyanofurane

1 (PDF)	DEFENSE TECHNICAL INFORMATION CTR DTIC OCA
2 (PDF)	DIR ARL RDRL CIO L IMAL HRA MAIL & RECORDS MGMT
1 (PDF)	GOVT PRINTG OFC A MALHOTRA
5 (PDF)	ARL RDRL WMM D E WETZEL RDRL WMM G J ANDZELM J LENHART R LAMBETH B RINDERSPACHER